Progress In Electromagnetics Research M, Vol. 84, 137–145, 2019

A Sparse-Based Clutter Suppression Methodology for Single Channel SAR

Xin Wang* and Teng Li

Abstract—A sparse imaging-based clutter suppression method for one channel synthetic aperture radar (SAR) is proposed in this paper. The Doppler characteristic differences between the radar received signal of clutter and moving targets are utilized in this method. A joint projection operator is formulated, and the norm constraint is employed to realize and promote clutter suppression. The reconstructed MT results with suppressed clutter can be applied to moving target detection and imaging. Numerical simulation can verify the validity and robustness of the proposed methodology.

1. INTRODUCTION

Ground moving target indication (GMTI) [1–3] in synthetic aperture radar (SAR) has received more and more interest in recent years. When there are multiple moving targets (MT) located inside a strong clutter in a single channel SAR, the implementation of GMTI becomes difficult. In this case, the undesirable clutter which will mask true MTs should be suppressed before detecting.

However, the degree of freedom in single channel SAR systems is limited, which affects the application of multi-channel clutter suppression methods [4–6]. The space Doppler adaptive processing (SDAP) operation [7] has been proposed to suppress a clutter by constructing virtual multi-channel data. Nevertheless, a high pulse repetition frequency is required in this method, and residual clutter still exists. Based on multi-look or sub-aperture imageries, interferometry [8], non-coherent subtraction [9], and low-rank matrix decomposition methods [10, 11] can be employed to suppress a clutter for GMTI. The phase information of sub-imageries is used in interferometry processing while the amplitude is utilized in the other two methods. However, the phase terms might be affected by noise and strong clutter in SAR data and thus degrade the performance of interferometry. Moreover, the amplitude information of MTs could be masked by strong clutters in low signal to clutter ratio (SCR) cases. The performance of no-coherent subtraction and low-rank matrix decomposition methods will thus degrade severely.

Generally, the Doppler modulation rate of MT is different from that of a static clutter. This has been used as the basis of GMTI processing after time-frequency analysis [12–14]. Though these methods fail to detect slow-moving objects located inside strong clutter regions, the Doppler rate differences can still be utilized to suppress clutters by applying some suitable regularization constraint. To solve the GMTI problem in single channel SAR, we propose a joint sparse-imaging based method for clutter suppression. Only one channel SAR signal is provided and used in this method. The mix-received SAR data will be separated, and clutters will be suppressed significantly by using a sparse constraint. The SAR signal model will be described and formulated in Section 2 firstly. Then, the joint sparse imaging methodology will be presented and discussed in Section 3. Finally, numerical simulations will verify that the algorithm can realize clutter suppression successfully.

Received 11 April 2019, Accepted 11 July 2019, Scheduled 27 August 2019

* Corresponding author: Xin Wang (wangx@njupt.edu.cn).
The authors are with the College of Telecommunications & Information Engineering, Nanjing University of Posts & Telecommunication, Nanjing 210003, China.

2. SAR SIGNAL MODEL

In a SAR system, a linear frequency modulated signal is generally used as the transmitted signal. The received radar back data after range compression can be denoted as

$$Y = C + F_m T_m + n_0, \tag{1}$$

where $Y \in R^{N_d \times 1}$ is a column vector derived by stacking the range compressed SAR data; $C \in R^{N_I \times 1}$ is the clutter; $T_m \in R^{N_I \times 1}$ corresponds to the radar cross section (RCS) of MT; $F_m \in R^{N_d \times N_I}$ is the radar projection operator of the illuminated MTs; and n_0 is the noise vector. The notations N_d and N_I are referred to as the length of radar data and imagery, respectively.

3. JOINT SPARSE-BASED CLUTTER SUPPRESSION

As radar data are a collection of the reflected electromagnetic waves from the illuminated static scene and moving objects, weak MT signal might be submerged by strong clutters in low SCR cases. An effective clutter suppression or separation method becomes necessary for the following GMTI operation. An imaging-based clutter suppression method is developed in this section by utilizing the Doppler characteristic differences between clutter and MT radar data. The detailed processing flow is given in the following discussions.

3.1. Mismatched Signal Model

Since the real velocities of MT are unknown, the exact expression of F_m cannot be derived directly. Instead, a mismatched radar projection operator F_{mis} is constructed and used here based on the initialized velocities $v'_x = v_x + \Delta v_x$ and $v'_y = v_y + \Delta v_y$. Notations v_x and v_x are real velocities of MT along x and y axes, respectively, and Δv_x and Δv_y are referred to as the initialized mismatched velocity errors. Radar signal model in Eq. (1) can then be rewritten as

$$\begin{aligned} Y &\approx C + F_{mis} T_m + n_0 \\ &= \widehat{F} T + n_0 \end{aligned}, \tag{2}$$

where

$$\widehat{F} = [F, F_{mis}]^T,$$

In Eq. (2), $\widehat{F} \in R^{N_d \times 2N_I}$ is the joint radar projection operator consisting of $F \in R^{N_d \times N_I}$ and F_{mis}; $F \in R^{N_d \times N_I}$ is the system operator of the illuminated static scene; and $T = [T_c, \varphi_{res} T_m]^T \in R^{2N_I \times 1}$ incorporates the static scene field T_c and MT field T_m. To implement imaging processing, we formulate the following optimization problem as

$$\begin{aligned} \widehat{T} &= \min_T J(T) \\ &= \min_T \left\| Y - \widehat{F} T \right\|_2^2 + \lambda_1 \|T\|_p^p, \end{aligned} \tag{3}$$

where $\|\cdot\|_p^p$ denotes ℓ_p norm, and λ_1 is a positive scaling parameter. In Eq. (3), the first term is a data fidelity term, which incorporates the SAR observation model in Eq. (1) and the RCS information of illuminated targets. The adoption of the data fidelity term aims to implement the inversion of radar back data while the second term implies prior information about the field T. Since the Doppler modulation rates of radar back data from static and moving targets are different, the clutter and MT signal in the mix-received radar data will thus be matched to distinct projection operators F and F_{mis}, respectively. The utilization of the ℓ_p norm in the second term in Eq. (3), which means a sparse constraint of T, can promote the separation of the static scene and MT and implement the suppression of artefacts and side lobe in the reconstructed results simultaneously. Hence, solving the optimization problem in Eq. (3) will finally result in the generation of a static-scene imagery and an MT imagery T_m with a suppressed clutter.

3.2. Iterative Solution

Many papers employ the ℓ_p norm with $p = 0$ to constrain the reconstructed result to be sparse. Greedy methodologies and iterative hard thresholding algorithm have been developed to solve this regularization problem approximately, whereas the accuracy of these methods will degrade as a mismatched MT radar projection operator F_{mis} is utilized in this paper. Moreover, the ℓ_1 norm relaxation is widely used instead of directly solving the ℓ_0 regularization problem. However, as discussed in [15], the ℓ_p norm with $0 < p < 1$ will result in a more sparse solution and thus is used in our method.

As ℓ_p norm is non-differentiable around the origin, the exact solution of Eq. (3) is difficult to be derived. The following approximation expression is applied instead

$$\|z\|_p^p \approx \sum_{i=1}^{N_z} \left(|z(i)|^2 + \varepsilon \right)^{p/2}, \tag{4}$$

where $\varepsilon \geq 0$ is a very small positive constant; N_z denotes the length of the vector z; $z(i)$ is referred to as the ith element in z. Substituting Eq. (4) into Eq. (3), a new cost equation can be derived as

$$J_m\left(T\right) = \left\| Y - \widehat{F}T \right\|_2^2 + \lambda_1 \sum_{i=1}^{N_z} \left(|T(i)|^2 + \varepsilon \right)^{p/2}, \tag{5}$$

The modified cost function $J_m(T)$ will be always close to $J(T)$ when $\varepsilon \to 0$ [15].

Based on the Hessian matrix approximation [12], the minimization of Eq. (5) can be solved according to the following iterative formula

$$\widehat{T}^{(n+1)} = \widehat{T}^{(n)} - \gamma \left[H\left(\widehat{T}^{(n)} \right) \right]^{-1} \nabla J_m\left(\widehat{T}^{(n)} \right), \tag{6}$$

where

$$H\left(\widehat{T}^{(n)} \right) 2\widehat{F}^H \widehat{F} + p\lambda_1 diag \left\{ \left(\left| \widehat{T}^{(n)}(j) \right|^2 + \varepsilon \right)^{p/2-1} \right\}, \tag{7a}$$

$$\nabla J_m\left(\widehat{T}^{(n)} \right) = H\left(\widehat{T}^{(n)} \right) \widehat{T}^{(n)} - 2\widehat{F}^H Y, \tag{7b}$$

In Eq. (6), γ denotes the iteration step; $\nabla J_m(\cdot)$ is the complex gradient of the cost function $J_m(T)$; $T^{(n)}$ is the estimation result after the nth iteration; $\left[H\left(\widehat{T}^{(n)} \right) \right]^{-1}$ is the inversion matrix of $H\left(\widehat{T}^{(n)} \right)$; and superscript H denotes the conjugate transposition of a matrix.

After substituting Eq. (7b) into Eq. (6), we can derive the following equation

$$\left[H\left(\widehat{T}^{(n)} \right) \right] \widehat{T}^{(n+1)} = (1-\gamma) \left[H\left(\widehat{T}^{(n)} \right) \right] \widehat{T}^{(n)} + 2\gamma\widehat{F}^H Y, \tag{8}$$

Neglecting the elements in $\widehat{F}^H \widehat{F}$ whose magnitudes are smaller than 1% of the largest element, we find that the coefficient $H\left(\widehat{T}_i^{(n)} \right)$ in Eq. (8) becomes a sparse conjugate coefficient matrix. Hence, the conjugate gradient method could be applied to search for the solution of Eq. (8). The real part and imaginary part of the range compressed data Y and the projection operator $\widehat{F}$ are stacked to derive two combinatorial vectors to compute the solution. When the converge condition is satisfied, MT imagery will be obtained by restacking operation.

3.3. Large Mismatched Error

In Section 3.2, field T is derived based on an initialized mismatched system operator F_{mis}. Owing to the ℓ_p norm constraint, the energy of clutter will be suppressed in the derived MT imagery when the mismatched velocity error is not too large, which can be verified by the numerical simulation in the next section. When the assumed velocities deviate from real values severely, the performance of data separation and clutter suppression might degrade. To solve this problem, we try to reduce the mismatched error after the iteration computation.

We discuss to update the MT radar projection operator F_{mis} to reduce the mismatched error. MT radar patch data reconstruction and Doppler parameter estimation operations are developed here to realize the updating. As the phase information is not retained in the joint sparse-based processing, the amplitude information of the results obtained after iteration computation might be combined with the phase term of the initialized imageries to produce the reconstruction. Then, the approximately constructed MT data will be used to update MT radar projection, which can be expressed as

$$\overset{\frown}{Y}_m^{(n)} = F_{mis}\left[\left|\overset{\frown}{T}_m^{(n)}\right| \odot \exp\left(\angle \overset{\frown}{T}_m^{(0)}\right)\right], \tag{9}$$

where $\odot$ denotes the elementwise product; $|\cdot|$ and $\angle\cdot$ indicate computing the amplitude and angle of vector; $\overset{\frown}{T}_m^{(n)}$ and $\overset{\frown}{T}_m^{(0)}$ are referred to as the constructed MT imagery after nth iteration and initialized MT imagery, respectively. The reconstructed data $\overset{\frown}{Y}_m^{(n)}$, which is an approximation of real MT radar data with suppressed clutter, can be used for accurate Doppler parameter estimation [16, 17]. Then, MT radar projection operator is updated to continue the subsequent iteration to output the results.

Considering that the response functions of MTs are usually distributed in small patches of SAR imagery, we do not need to use the original radar data directly. The patch decomposition operation, which can be acquired by motion compensation, filtering, and down-sampling operations [18], will be employed to improve the efficiency. In practical data processing procedure, the size of MT patch is generally very small (the patch size for one MT might be restricted as 30 × 30 in some cases). The computational burden in joint sparse imaging thus will be reduced significantly, much lower than that of frequency domain imaging processing of original radar data. The detailed processing flow is listed in Algorithm 1 and depicted in Fig. 1.

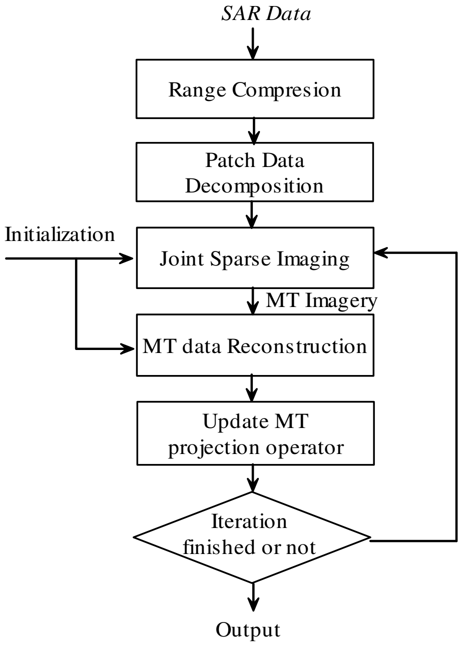

Figure 1. Joint sparse-based clutter suppression.

Algorithm 1 Joint sparse-based clutter suppression.

```
1: Input: Range compressed radar patch data, joint radar projection operator;
2: Initialization: $\overset{\frown}{T}^{(0)}$ $\overset{\frown}{F}^{(0)}$, $\lambda_1$, $\gamma$, $p$;
3: While not converge do
4: Update $\overset{\frown}{T}^{(n+1)}$ according to Eq. (8);
5: End
6: Update MT projection operator based on Doppler parameter estimation results of the reconstructed
   MT radar data;
7: Repeat step 3–5.
8: Output
```

4. SIMULATION

In this section, numerical simulations will be performed to verify the proposed joint sparse-based algorithm, where the parameters are given in Table 1. Radar back data from 4 ground moving targets, marked as MT1-4 in Fig. 2(a), are simulated. The range compressed SAR data combined with and without clutter are given in Fig. 2(b) and Fig. 2(c), respectively.

Table 1. Simulation parameters.

Carrier frequency	10 GHz
Range bandwidth	300 MHz
Resolution in x dimension	0.41 m
Resolution in y dimension	0.23 m

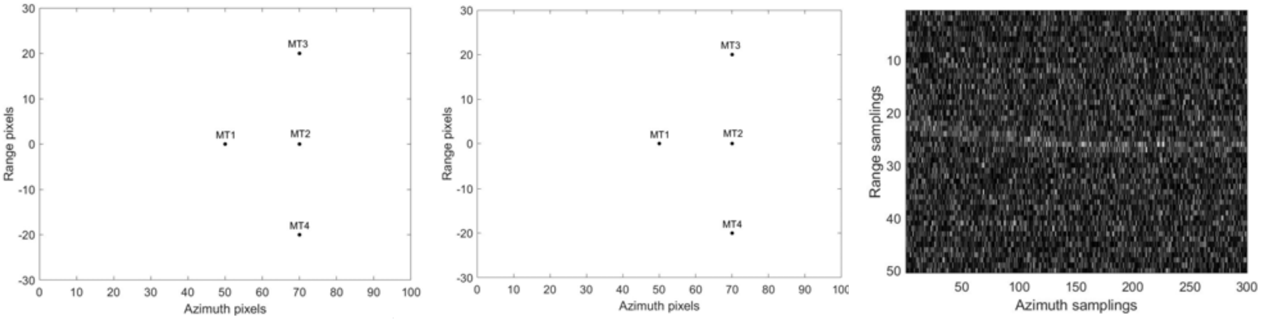

(a) (b) (c)

Figure 2. MTs and radar data. (a) 4 MTs; (b) Range compressed radar data combined with clutter; (c) Range compressed MT data without clutter.

The velocities and positions of simulated MTs are listed in Table 2, and the imaging results after traditional matched filtering (MF) processing are given in Fig. 3(a) and Fig. 3(b). As the motion of MTs is not considered in MF processing, smearing and geometry deviation emerge in the constructed SAR imagery, as shown in Fig. 3(b), where the five ellipses indicate the locations of defocused MTs. The SCR values of MTs, which are calculated as the ratio of the energies of MT and clutter in SAR imagery, are listed in Table 2. It can be seen from Table 2 and Fig. 3(b) that most of the energies of MT3 and MT3 are masked by the clutter which should be suppressed before detecting and MT refocusing.

Here, for comparison, the non-coherent subtraction, interferometry, and our joint sparse-based processing are performed on the defocused MT imagery in Fig. 3(b), respectively. It can be seen from Fig. 3(c) and Fig. 3(d) that the clutter is suppressed after subtraction and interferometry operations,

Table 2. MT simulation parameters.

	MT1	MT2	MT3	MT4
Azimuth position(pixel)	30	70	70	70
Range position(pixel)	30	30	10	50
v_x	17 m/s	22 m/s	21 m/s	21 m/s
v_y	0.8 m/s	0.8 m/s	0.8 m/s	0.8 m/s
SCR	8 dB	3 dB	−4 dB	−7 dB
Initialized Doppler Rate Error	20.04 Hz/s	9.81 Hz/s	9.98 Hz/s	9.93 Hz/s
Updated Doppler Rate Error	0.04 Hz/s	0.01 Hz/s	0.02 Hz/s	0.02 Hz/s

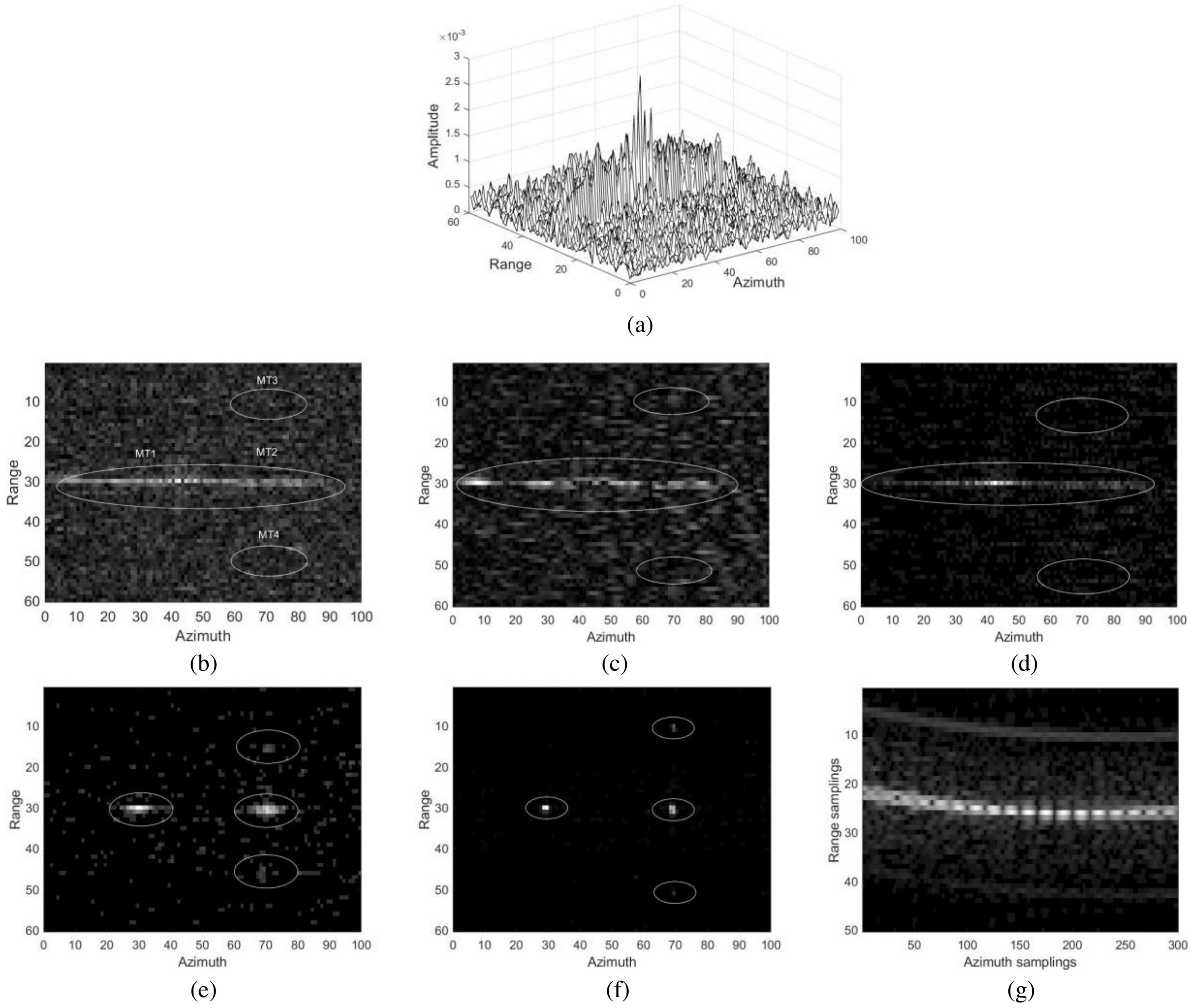

(a) (b) (c) (d) (e) (f) (g)

Figure 3. MF and sparse imaging result. (a) Three-dimensional figure of MT imagery; (b) SAR MT imagery; (c) Imagery result derived by non-coherent subtraction; (d) Imagery result after interferometry; (e) Imagery derived based on the initialized parameters; (f) and (g) Reconstructed MT imagery and radar data after joint sparse imaging.

but weak MTs are still difficult to be detected. In the joint sparse-based processing, two initialized velocities v'_x and v'_y, which are defined as 25 m/s and 0 m/s, are used in the first iteration to formulate the MT radar projection matrix. Though the initialized MT operator is mismatched, most of the energy

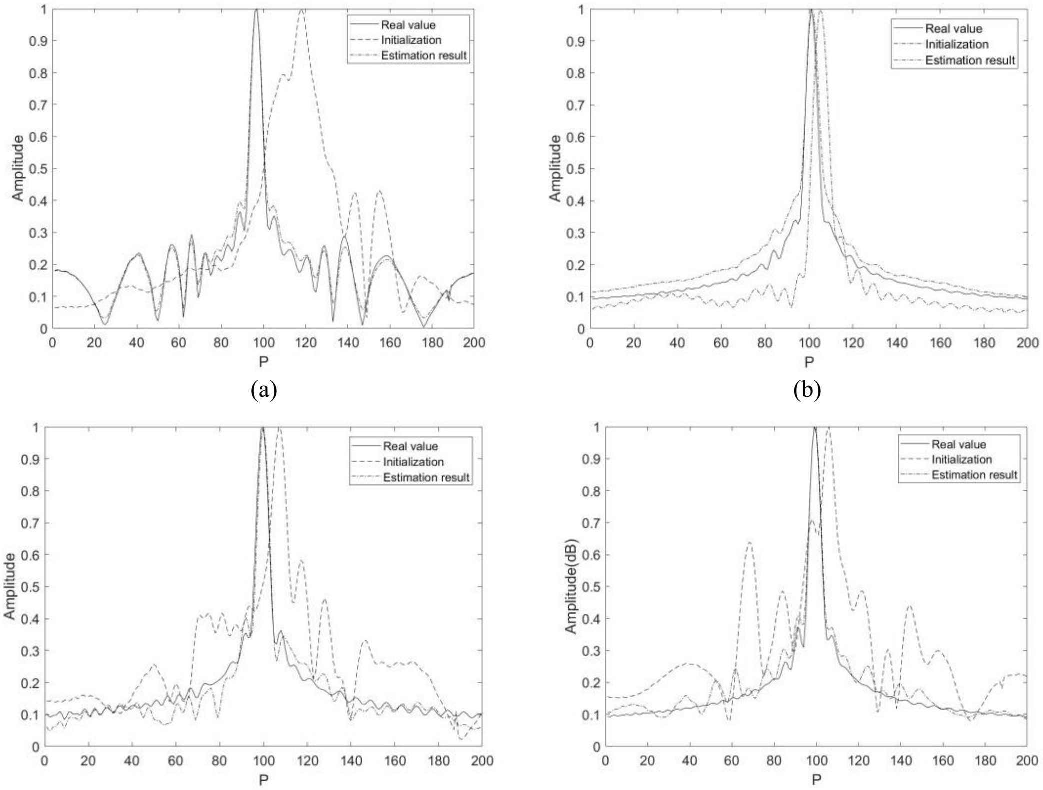

(a) (b)

(c) (d)

Figure 4. Doppler rate estimation results based on the reconstructed MT patch data. (a) MT1; (b) MT2; (c) MT3; (d) MT4.

of the clutter is still suppressed in the imagery derived after iteration, as shown in Fig. 3(d). MT radar patch data are then reconstructed based on Eq. (9), and Doppler parameter estimation is performed after keystone transform and range cell migration correction. The fractional Fourier transform is used for estimation, and the results are given in Fig. 4. We can find from this figure that the Doppler rate derived from reconstructed MT patch data is very close to the real values which are obtained from the simulated phase history of MT without clutter. Finally, updating the MT system operator based on the computed Doppler parameters, we can get the MT imagery and radar patch data with significantly reduced clutter, as shown in Figs. 3(f) and 3(g). To further verify our method, the azimuth profiles of the 4 MTs in the defocused SAR imagery and the results derived by subtraction, interferometry, and our method are depicted in Fig. 5. It could be concluded from these figure that our joint sparse-based algorithm can implement the suppression of clutter effectively, and the values of SCR are decreased to around 60 dB–80 dB.

Moreover, radar signal illuminated from 3 MTs with velocities 13 m/s and 1.8 m/s along azimuth and range dimensions combined with real SAR data (provided by AFRL) is processed by our method. The scene imagery is given in Fig. 6(a), where the white rectangular frames indicate the positions of the defocused MTs. Patch decomposition operation is employed on the original radar data, where the obtained sub-imagery and radar patch data are given in Figs. 6(b) and 6(c), respectively. In these two figures, most of the energy of MTs is masked by clutters. The joint sparse-based processing is then used to process the radar patch data with the initialized velocities $v_x' = 18\,\mathrm{m/s}$ and $v_x' = 0\,\mathrm{m/s}$. The obtained MT imagery based on the initialized velocities is depicted in Fig. 6(d), in which residual clutter still exists as a result of the utilization of a mismatched radar projection operator. After MT data reconstruction and radar system operator updating, MT imagery and radar data can be derived as Figs. 6(e) and 6(f). It can be seen from Figs. 6(e) and 6(f) that the clutter is suppressed significantly, which further verifies the validity of our method.

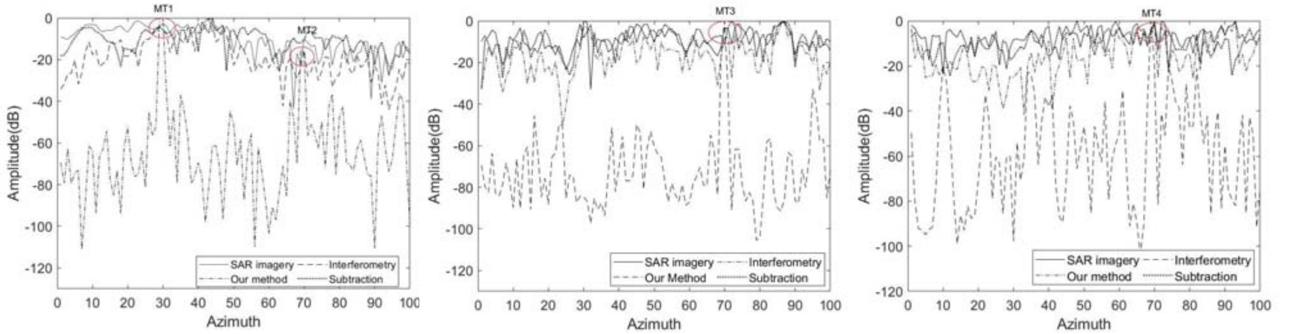

(a) (b) (c)

Figure 5. Comparison of azimuth profiles of MTs before and after clutter suppression. (a) MT1 and MT2; (b) MT3; (c) MT4.

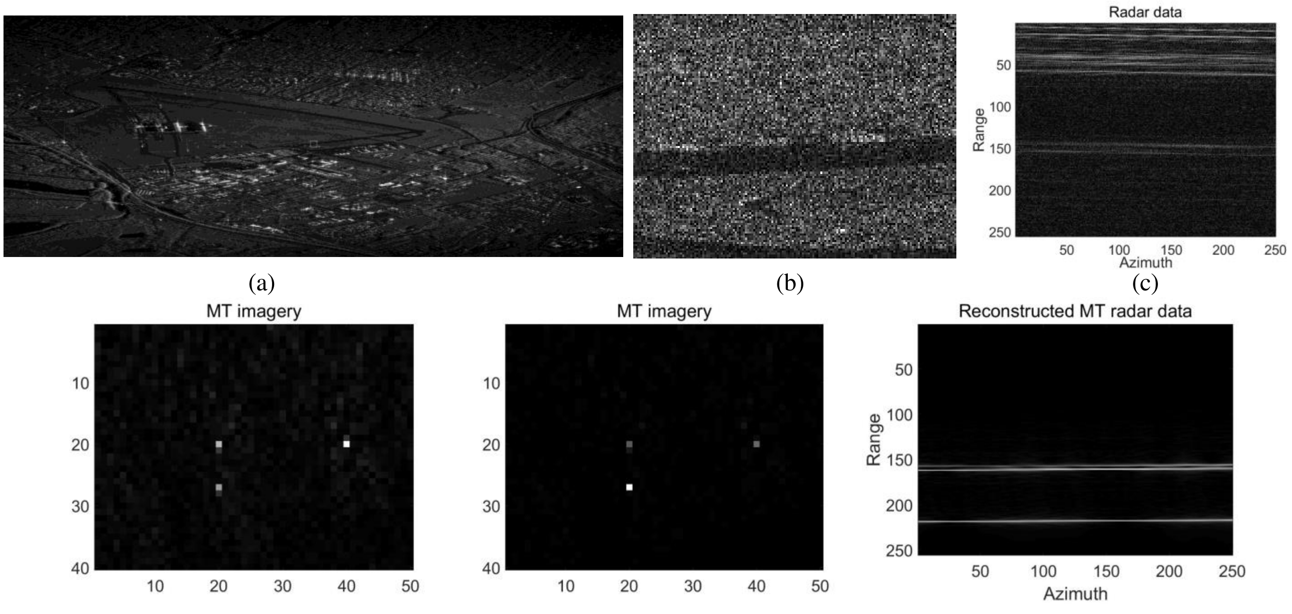

(a) (b) (c)

(d) (e) (f)

Figure 6. MF and sparse imaging result. (a) Scene imagery; (b) Enlarged rectangular area in Fig. 5(a); (c) Decomposed radar back data of rectangular area in Fig. 6(a); (d) Reconstructed MT imagery based on the initialized parameters; (e) and (f) Reconstructed MT imagery and radar data after joint sparse imaging.

5. CONCLUSION

A clutter suppression methodology based on joint sparse imaging is proposed in this paper. Due to the lack of moving parameters, an initialized mismatched MT radar projection operator is used in the iteration computation. Even so, the strong clutter will be suppressed significantly in the derived results as MT data reconstruction and projection operator update is employed in our method. The derived MT imagery and patch data with suppressed clutter can be used for detecting, imaging, and parameter estimation directly. In our method, a fixed regularization coefficient is used in the iteration. How to choose the regularization coefficient to promote the performance of data separation will be our future work.

ACKNOWLEDGMENT

This work was supported by the National Natural Science Foundation of China (61801232) and the Natural Science Foundation of Jiangsu Province (BK20160915).

REFERENCES

1. Curlander, J. C. and R. N. McDonoug, *Synthetic Aperture Radar*, Wiley, New York, 1991.
2. Kaan, D. and Y. Birsen, "Moving target artifacts in Bistatic synthetic aperture radar images," *IEEE Transactions on Computational Imaging*, Vol. 1, No. 1, 30–43, 2015.
3. Li, Z. Y., J. J. Wu, Q. Y. Yi, et al., "Bistatic forward-looking SAR ground moving target detection and imaging," *IEEE Transactions on Aerospace and Electronic Systems*, Vol. 51, No. 2, 1000–1026, 2015.
4. Zhang, S. X., M. D. Xing, X. G. Xia, et al., "Robust clutter suppression and moving target imaging approach for multichannel in azimuth high-resolution and wide-swath synthetic aperture radar," *IEEE Transactions on Geoscience and Remote Sensing*, Vol. 53, No. 2, 687–709, 2015.
5. Cerutti-Maori, D. and I. Sikaneta, "A generalization of DPCA processing for multichannel SAR/GMTI radars," *IEEE Transactions on Geoscience and Remote Sensing*, Vol. 51, No. 1, 560–572, 2013.
6. Li, J., Y. Huang, G. Liao, et al., "Moving target detection via efficient ATI-GoDec approach for multichannel SAR system," *IEEE Geoscience and Remote Sensing Letters*, Vol. 13, No. 9, 1320–1324, 2016.
7. Gelli, S., A. Bacci, D. A. Gray, et al., "Virtual multichannel SAR for ground moving target imaging," *IET Radar, Sonar and Navigation*, Vol. 10, No. 1, 50–62, 2016.
8. Jin, P., Y. Shi, et al., "A sub-aperture detection algorithm for single channel SAR-GMTI," *Chinese Journal of Electronics*, Vol. 4, 749–753, 2009.
9. Zhang, L., H. D. Guo, C. M. Han, et al., "Moving targets detection in SAR images based on sub-aperture decomposition," *Acta Electronica Sinica*, Vol. 36, No. 6, 12101–1213, 2008.
10. Yin, J. P., U. Christine, S. Marc, et al., "Radar target and moving clutter separation based on the low-rank matrix optimization," *IEEE Transactions on Geoscience and Remote Sensing*, Vol. 56, No. 8, 4765–4780, 2018.
11. Yasin, M., M. Cetin, and A. S. Khwaja, "SAR imaging of moving targets by subaperture based low-rank and sparse decomposition," *2017 25th Signal Processing and Communications Applications Conference*, 2017.
12. Sun, H. B., G. S. Liu, H. Gu, et al., "Application of the fractional Fourier transform to moving target detection in airborne SAR," *IEEE Transactions on Aerospace and Electronic Systems*, Vol. 38, No. 4, 1416–1424, 2002.
13. Barbarossa, S., "Doppler-rate filtering for detecting moving targets with synthetic aperture radars," *Proceedings of SPIE The International Society for Optical Engineering*, Vol. 1101, 140, 1989.
14. Yu, X., X. Chen, Y. Huang, et al., "Radar detection for moving target in short-time sparse fractional representative domain," *Systems Engineering and Electronics*, Vol. 40, No. 11, 2426–2432, 2018.
15. Cetin, M. and W. C. Karl, "Feature-enhanced synthetic aperture radar image formation based on nonquadratic regularization," *IEEE Transactions on Image Processing*, Vol. 10, No. 4, 623–631, 2001.
16. Huang, P., G. Liao, Z. Yang, et al., "Ground maneuvering target imaging and high-order motion parameter estimation based on second-order keystone and generalized Hough-HAF transform," *IEEE Transactions on Geoscience and Remote Sensing*, Vol. 55, No. 1, 320–335, 2017.
17. Mao, X., "SAR imaging of moving target based on knowledge-aided two-dimensional autofocus," *Computer Science*, 2015.
18. Wahl, D. E., D. A. Yocky, and C. V. J. Jakowatz, "An implementation of a fast backprojection image formation algorithm for spotlight-mode SAR," *Proceeding of SPIE*, Vol. 6970, No. 8, 2008.